


Subwavelength Sound Focusing and Imaging Via Gradient Metasurface-Enabled Spoof Surface Acoustic Wave Modulation

Tuo Liu,^{1,2} Fei Chen,^{1,2} Shanjun Liang,^{1,2} He Gao,² and Jie Zhu^{1,2,*}

¹The Hong Kong Polytechnic University Shenzhen Research Institute, Shenzhen 518057, P.R. China

²Department of Mechanical Engineering, The Hong Kong Polytechnic University, Hung Hom, Kowloon, Hong Kong SAR, P.R. China

 (Received 5 October 2018; revised manuscript received 14 January 2019; published 26 March 2019)

Manipulating acoustic waves beyond the diffraction limit offers alternative possibilities to many applications in wave physics. Here, we show that a gradient-index acoustic metasurface is able to achieve this purpose by modulating airborne sound at subwavelength scales via the local-resonance-controlled spoof surface acoustic waves. From the dispersion relation of such a surface mode, a design approach of explicitly correlating the effective refractive index with the geometrical unit-cell parameters can be obtained. With one carefully designed gradient-index acoustic metasurface constructed using locally resonant elements, we demonstrate the experimental realizations of both subwavelength plane-wave sound focusing and super-resolution acoustic imaging. This work provides a feasible pathway to the subwavelength manipulation of airborne sound. Moreover, it offers an ideal experimental platform to directly observe how acoustic energy flow is governed by refractive-index modulation. The proposed design approach can be easily applied to various spoof surface acoustic wave devices that demand gradient index distribution.

DOI: [10.1103/PhysRevApplied.11.034061](https://doi.org/10.1103/PhysRevApplied.11.034061)

I. INTRODUCTION

Diffraction fundamentally limits the behavior of classical waves. Things such as the spatial resolution of an imaging system or the minimum focal spot size are, therefore, bounded due to the fact that near-field evanescent waves carrying rich subwavelength information decay exponentially away from the object and/or source region. Overcoming this barrier with subdiffraction-limited techniques, even only for an acoustic system, would benefit a wide variety of applications ranging from seismic exploration and sonic well logging, to ultrasonic nondestructive evaluation and biomedical imaging and therapy. Therefore, following the proposals of superlens and hyperlens in optics [1–5], acoustic metamaterials with negative properties [6–11] or extremely anisotropic properties [12–20] have been reported to circumvent the diffraction limit through amplifying the evanescent waves or converting or magnifying them into propagating modes inside or outside the metamaterials. An alternative strategy was developed to combine time-reversal mirrors with an acoustic sink or a resonators' array [21–23], allowing flexible control of a sound field and recovery of evanescent waves based on an inversion procedure. It has also been shown that by designing the plane-wave band gap and trapped resonances of an acoustic metamaterial within the same band, low-spatial-frequency components can be filtered so that

only evanescent waves are utilized to create the edge-based image with subwavelength resolution [24]. However, specific to experimental realization of subwavelength sound focusing, previous works either rely on additional time-reversal techniques [21–23], or require the sound source to be closely attached to the lens [10,11]. Although Maznev *et al.* have pointed out that the time-reversal technique is not the sole factor responsible for the sharp focal spot [25,26], it still plays an indispensable role in the focusing process control. Most importantly, none has demonstrated the capability to focus plane acoustic waves in the subwavelength regime, which corresponds to the spatial Fourier transform essential for not only many imaging systems, but also the minimization of metamaterial-based analog computing devices [27–29].

As a counterpart of spoof surface plasmon polaritons [30,31], spoof surface acoustic waves [22,25,32–51] (SSAWs) bring fresh possibilities to the subwavelength manipulation of airborne sound, benefitting from their high-spatial-frequency feature. SSAWs are a type of surface acoustic mode guided by periodically corrugated, perforated, or resonator-embedded surfaces. The subwavelength feature of SSAW can be well understood from the dispersion relation $k_{\parallel}^2 + k_{\perp}^2 = k_0^2$, where k_{\parallel} and k_{\perp} are the in-plane and out-of-plane wave-vector components, and k_0 is the wavenumber of airborne sound in free space. Since the surface mode is evanescent along the vertical direction, k_{\perp} is an imaginary number so that k_{\parallel} is allowed to be much larger than k_0 , which indicates the compressed

*jie.zhu@polyu.edu.hk

wavelength of SSAW and its capability to carry subwavelength information. The SSAW's dispersion characteristics can be engineered by adjusting the structural geometry to provide the desired artificial boundary conditions, enabling many fascinating functionalities such as beam collimation [33,35,43,45], subwavelength focusing and/or imaging [22,25,38,39], rainbow trapping [40–42,49], topological insulators [48], and so on. More intriguingly, the enhanced and confined sound field of SSAWs is open to the environment and measurable even away from the surface, which suggests a platform with great potential to intuitively observe acoustic wave guiding and energy flow at subwavelength scales.

Taking advantage of such exceptional properties of SSAWs, we present a systematical design approach of gradient-index (GRIN) acoustic metasurfaces to manipulate and observe airborne sound at subwavelength scales. Unlike the previous study that adjusts the interaction strength among shallow cavities through the hole diameter to obtain the GRIN distribution [39], here the unit-cell hole depth is used as a unique and direct variable. In essence, it is able to control the local resonance behavior of individual units rather than the mutual coupling among them, so that a broad range of effective refractive indices become available, which fundamentally deepens the subwavelength scale one may reach. We also note that the index-depth correlation can be analytically expressed in an explicit form. This simplifies the design process and allows much freedom in terms of the effective index modulation, which may facilitate the development of innovative acoustic devices for focusing, imaging, sensing, and so on.

We thoroughly examine the effectiveness of the systematical design approach by considering a case of hyperbolic secant index profile [52,53]. As conceptually illustrated in Fig. 1, the GRIN metasurface is able to support

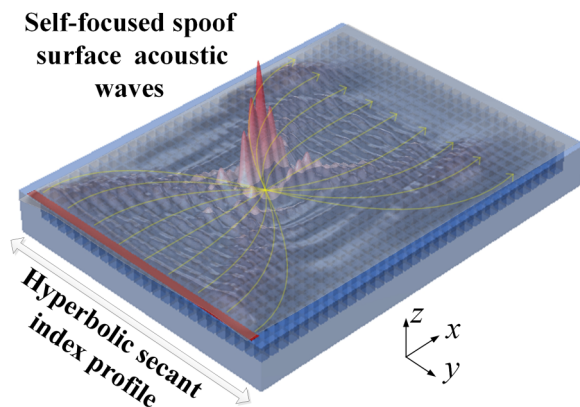


FIG. 1. The gradient-index metasurface and the self-focusing of spoof surface acoustic waves. The gradient-index metasurface offers a hyperbolic secant refractive-index profile to the structure-induced spoof surface acoustic waves. The yellow lines denote the trajectories of the incident sound waves.

self-focused SSAWs converted from incident plane waves. A focal spot with a FWHM less than 1/7 of the free-space wavelength is observed. In addition, subwavelength acoustic imaging is also experimentally realized through coupling the nonpropagative evanescent field of the source into the traveling SSAWs with large wave vectors.

II. METHODS

Numerical simulations (finite element method, FEM) throughout the article are performed using the pressure acoustics module of COMSOL Multiphysics. The simulated dispersion relations [Figs. 2(b) and 2(c)] are obtained by calculating the eigenfrequencies of the unit cell for different wave-vector values. The simulation model consists of a single square hole and a cuboid region above it. Floquet periodic boundary conditions are applied in the two horizontal directions (x and y) of the cuboid region while rigid-wall boundary conditions are used for all other boundaries. The top wall of the simulation domain is sufficiently far away from the hole to guarantee an accurate calculation of the surface mode [25] (scattering boundary condition also works [48]). The sound fields of the lossless continuous GRIN medium (based on our design in Fig. 3) as given by Figs. 4(a) and 4(b) are obtained from a two-dimensional full-wave simulation in the frequency domain. The ideal GRIN distribution is implemented by setting a continuous variation of the speed of sound along the transverse direction y based on the hyperbolic secant function $n(y) = n_0 \operatorname{sech}(\alpha y)$. The results of the GRIN metasurface [Figs. 4(c)–4(h)] are obtained from three-dimensional full-wave simulation in the frequency domain. The linelike sound source is accomplished by applying a plane-wave-radiation condition on a $10 \times 380 \text{ mm}^2$ area. The inherent losses inside the holes are considered by replacing the purely real physical properties of air with frequency-dependent complex quantities. The physical properties of air at 20°C , standard atmospheric pressure are: density $\rho_0 = 1.21 \text{ kg/m}^3$, speed of sound $c_0 = 343 \text{ m/s}$, thermal conductivity $\kappa = 0.0258 \text{ W/(m K)}$, viscosity $\mu = 1.81 \times 10^{-5} \text{ kg/(m s)}$, the specific heat at constant pressure $C_p = 1.005 \times 10^3 \text{ J/(kg K)}$, and the ratio of the specific heats $\gamma = 1.4$. For the simulations of the two-dimensional subwavelength imaging, an infinitely large interior rigid boundary with a C-shaped opening is placed between the linelike source and the metasurface. A set of models for different vertical positions of the C-shaped opening is simulated to extract the energy-density distributions, during which the step is 5 mm .

For our experimental verification, a lock-in amplifier (Zurich Instrument HF2LI) controlled by the computer is used for signal generation and acquisition [54]. It sends sinusoidal signals to a loudspeaker box via an audio power amplifier (Brüel & Kjær, Type 2716C) to generate acoustic waves. The loudspeaker box has a 10-mm wide, 380-mm

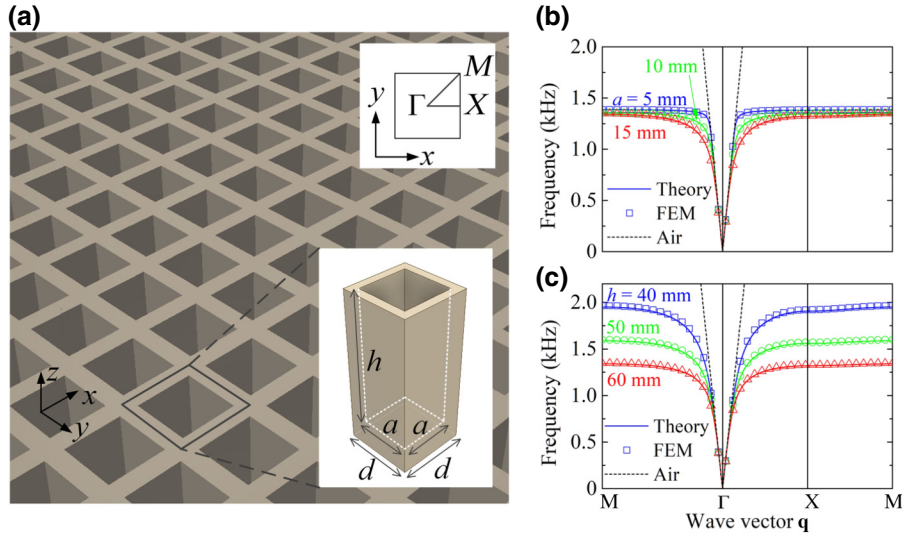


FIG. 2. Geometry governed dispersion characteristics of the spoof surface acoustic waves. (a) Schematic illustration of the metasurface perforated with uniform square holes. The lower-right inset shows the unit cell, in which the side length and depth of the square hole are a and h , with a lattice constant of d . The upper-right inset is the corresponding first Brillouin zone. (b) Dispersion curves for different side lengths ($a = 5, 10, 15$ mm) with fixed hole depth $h = 60$ mm and lattice constant $d = 20$ mm. (c) Dispersion curves for different hole depths ($h = 40, 50, 60$ mm) with fixed side length $a = 15$ mm and lattice constant $d = 20$ mm. The solid lines and symbols represent the theoretical and numerical results, respectively, while colors are used to distinguish different a or h . The dispersion of sound waves in free space air is denoted by the dashed black line.

long slit that acts as a linelike source, which consists of 9 1.5-inch full-range loudspeaker units (Peerless by Tymphany, PMT-40N25AL01-04). The sound field above the metasurface sample is measured by a 1/4-inch free-field microphone with a built-in preamplifier (Brüel & Kjær, Type 4935), mounted on a two-dimensional moving stage. The recorded signals are sent back to the lock-in amplifier via a conditioning amplifier (Brüel & Kjær, NEXUS Type 2693A). The measured sound fields of Figs. 5(a)–5(c) are obtained following a similar procedure, in which a pair of loudspeaker boxes, each with a very small opening, are used as pointlike sources. For scanning measurement of the two-dimensional image plane, a thin rigid plate carved with a C-shaped opening is inserted between the linelike source and the metasurface sample. The carved plate is several times larger than the wavelength to suppress diffraction at the plate edges. It is 10 mm away from both the speaker box and the metasurface sample so that sound radiation is relatively stable for different scanning heights. The scanning height is controlled by adjusting the vertical position of the C-shaped opening, during which the energy-density distribution 10 mm above the metasurface sample is measured for each scanning height. The results are then synthesized to produce Fig. 5(f).

III. CORRELATING THE EFFECTIVE INDEX WITH THE HOLE DEPTH

As depicted in Fig. 2(a), the SSAW metasurface consists of periodically perforated square holes with

deep-subwavelength openings, forming a two-dimensional array of quarter-wavelength resonator unit cells. The side length and depth of the holes are, respectively, a and h . The lattice constant is d . When the metasurface is immersed in air of density ρ_0 and speed of sound c_0 , for the lossless case, the dispersion relation of the supported SSAWs takes the form [49]

$$1 - k_0 \tan(k_0 h) \frac{a^2}{d^2} \sum_{m,n=-\infty}^{+\infty} \frac{S_{mn}^2}{\sqrt{(q^{(m,n)})^2 - k_0^2}} = 0, \quad (1)$$

where $k_0 = 2\pi f/c_0$ is the wavenumber in air with f being the frequency, and $S_{mn} = \text{sinc}(k_x^{(m)} a/2) \text{sinc}(k_y^{(n)} a/2)$.

$q^{(m,n)} = \sqrt{(k_x^{(m)})^2 + (k_y^{(n)})^2}$ is the in-plane wave vector of the (m,n) th-order diffracted wave with $k_x^{(m)} = k_x + (2\pi m/d)$ and $k_y^{(n)} = k_y + (2\pi n/d)$, $m, n \in \mathbf{Z}$. $q = \sqrt{k_x^2 + k_y^2}$ is the Bloch wave vector in the first Brillouin zone, satisfying the condition $q > k_0$ for a surface mode propagative within the xy -plane while being evanescent along the transverse direction. It corresponds to the propagation constant of the SSAWs.

SSAWs originate from the interaction between the local oscillation inside individual holes and the mutual coupling among neighboring ones. Their propagation characteristics are governed by the geometrical parameters. We calculate the dispersion relations of different h and a values for a fixed lattice constant $d = 20$ mm along the high-symmetry

orientations of a square lattice [inset of Fig. 2(a)] using Eq. (1), and compare them with the FEM simulation results. The material properties are set as $\rho_0 = 1.21 \text{ kg/m}^3$ and $c_0 = 343 \text{ m/s}$, respectively. As presented in Figs. 2(b) and 2(c), the theoretical results agree well with the simulation results. The dispersion curves asymptotically approach the air line at a very low-frequency range. They start to deviate below the “sound cone” with the increase of frequency, until becoming flat at the edge of the first Brillouin zone. Geometrical parameters including d and h affect the curve shape and band edge, namely, the propagation characteristics of the surface mode. The former one mainly controls the coupling strength among units while the latter one governs the local resonance behavior. For large h/d values, the band edge appears in the low-frequency regime owing to the dominating local resonance within the unit cell, indicating the possibility of airborne sound manipulation at a subwavelength scale. It should be noted that the difference between the wave vectors in the ΓX and ΓM directions gradually emerges as the frequency approaches the edge of the first Brillouin zone, leading to directional effective properties (noncircular equifrequency contour) and a narrow partial band gap at even higher frequencies [38]. In addition, the effect of thermal and viscous losses also becomes non-negligible near the band edge. Yet the dissipation and effective index change can be alleviated by carefully selecting the geometrical parameters and operating frequencies [54].

Based on the dispersion relation, we may build a straightforward mapping relationship between the geometrical parameters and the effective refractive index $n_{\text{eff}} = q/k_0$. The maximum effective refractive indices along the high symmetry orientations ΓX and ΓM are $n_{\Gamma X, \text{max}} = \lambda/2d$ and $n_{\Gamma M, \text{max}} = \lambda/\sqrt{2}d$, respectively, where λ is the wavelength of airborne sound. It suggests to what degree the SSAWs can be compressed and the highest spatial frequency can be achieved in theory. If we focus on the frequency range slightly away from the band edge, the approximation $n_{\text{eff}} \approx n_{\Gamma X} \approx n_{\Gamma M}$ is valid, and hence Eq. (1) can be rewritten as

$$h = \frac{1}{k_0} \arctan \left(\frac{1}{k_0} \frac{d^2}{a^2} \left(\sum_{m,n=-\infty}^{+\infty} \frac{\text{sinc}^2(K_m a/2) \text{sinc}^2(K_n a/2)}{\sqrt{K_m^2 + K_n^2 - k_0^2}} \right)^{-1} \right), \quad (2)$$

where $K_m = (\sqrt{2}/2)n_{\text{eff}}k_0 + (2\pi m/d)$ and $K_n = (\sqrt{2}/2)n_{\text{eff}}k_0 + (2\pi n/d)$. Equation (2) provides a distinct analytical solution to correlate the effective refractive index with the hole depth. When a and d are fixed, we can now unequivocally obtain the required unit-cell hole depth, given the value of the refractive index ($n_{\text{eff}} \geq 1$). This significantly simplifies the SSAW metasurfaces' design procedure [55] and allows flexible refractive-index adjustment due to the local-resonance-induced dispersion

behavior, especially for the cases that require gradient-index distribution.

IV. GRADIENT-INDEX DESIGN

Realizing a planar GRIN lens that can focus acoustic waves requires the construction of a specific refractive-index profile along the direction transverse to wave propagation. Assume that x and y , respectively, denote the propagating and transverse directions, as illustrated in Fig. 1. Here, we adopt the hyperbolic secant index distribution [52,53] $n(y) = n_0 \text{sech}(\alpha y)$, where n_0 is the refractive index at the center axis $y = 0$, and α is the gradient coefficient. In this scenario, an incident plane wave traveling along the x direction would gradually converge toward the central axis to form a focusing spot, and then redirect into a planar SSAW beam. The trajectory follows a sinusoidal path, and the focal length is analytically given by $L_{\text{focal}} = \pi/2\alpha$.

With the proposed correlation Eq. (2), we are able to calculate the depth of each unit-cell hole required by the hyperbolic secant index distribution. A $25(x) \times 19(y)$ elements GRIN metasurface that enables SSAW focusing is designed. The side length of the holes and the lattice constant are fixed with $a = 15$ and $d = 20$ mm, respectively. The transverse-hole-depth distribution as a function of y is presented in Fig. 3(c). It is determined directly from Eq. (2) according to the refractive-index profile of $n_0 = 3.13$ and $\alpha \approx 8.27$ [see Fig. 3(d)]. The deepest holes are at the central axis with depth $h|_{y=0} = 60$ mm. The operating frequency is $f = 1250$ Hz. The designed focal length is $L_{\text{focal}} = 190$ mm. We plot the local dispersion relations corresponding to those individual unit-cell holes in Fig. 3(e). The hole depth can well control the local resonance behavior of individual units to tailor the dispersion curves and thus introduces a graded distribution of effective refractive index. It is worth mentioning that, as a result of the resonance-induced dispersion, the effective refractive-index profile of the acoustic metasurface is frequency dependent. For operating frequencies other than 1250 Hz, the index profile would inevitably shift away from the designed one, yet it still approximately fits the function $n(y) = n_0 \text{sech}(\alpha y)$ with specific n_0 and α .

The sample exhibited in Fig. 3(a) is fabricated using a three-dimensional printing technique (stereolithography), with the material (photosensitive resin) being very rigid compared to air. The last five columns of holes ($400 \text{ mm} \leq x \leq 500 \text{ mm}$) are filled with sound-absorption materials to mimic a reflectionless boundary for the SSAWs. The entire sound field near the metasurface sample is measured point-by-point utilizing a 1/4-inch free-field microphone. In full-wave simulation, a linelike sound source is placed near the sample at $x = -10$ mm to effectively generate the incident SSAWs [36,39,44,45]. Experimentally, such a source is implemented through a loudspeaker

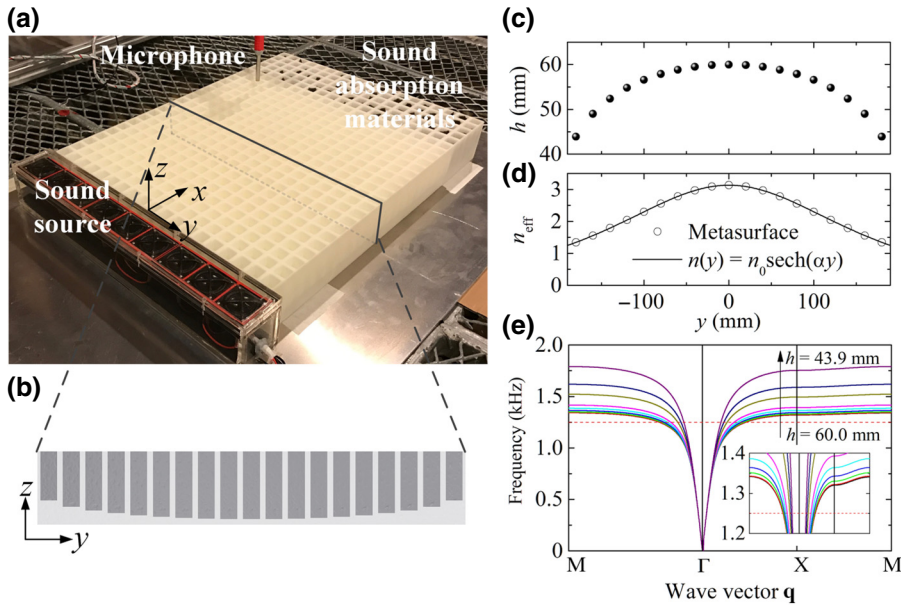


FIG. 3. Design of the gradient-index metasurface. (a) The metasurface sample and the experimental setup. (b) Schematic illustration of the graded square holes in the yz -plane. (c) Hole-depth distribution along the y direction. (d) Effective refractive-index distribution at 1250 Hz along the y direction. The solid line is the exact hyperbolic secant index profile of our design, in which $n_0 = 3.13$ and $\alpha = 8.27$, corresponding to a focal length of $L_{\text{focal}} = 190$ mm. (e) Local dispersion curves of the unit cells used in our design. Different colors denote different hole depths ranging from 43.9 to 60.0 mm. The inset is an enlarged plot of the curves around 1250 Hz.

box with a single slit, which can be seen in Fig. 3(a). Note that plane acoustic waves in free space can be coupled to the SSAWs via additional gratings [45,46] or a gradient transition [40,41,49,51]. Hence, the focusing process does not necessarily require near-field excitation. The thermal and viscous losses that inherently exist inside the holes are also considered [47,49] in our full-wave simulations.

V. SUBWAVELENGTH FOCUSING OF AIRBORNE SOUND

The designed acoustic GRIN metasurface has the unique capability to focus plane acoustic waves into a subwavelength hot spot by making full use of the hole-depth-governed local resonances. It is supported by the simulated and measured acoustic fields shown in Fig. 4. To validate our design approach, here, the result of an ideal two-dimensional continuous medium that satisfies the target GRIN distribution previously displayed in Fig. 3(d) is also presented for comparison [see Figs. 4(a) and 4(b)]. At the designed operating frequency of 1250 Hz, the overall experimental and simulation results of the GRIN metasurface [see Figs. 4(c)–4(f)] agree very well with each other. Both of them are consistent with the ideal case of a lossless GRIN medium, except that a moderate attenuation of SSAW due to the inherent losses weakens the overall sound field along the wave propagation direction. The incident plane wave traveling from left to right gradually bends toward the central axis and converges to a small spot at around $x = 190$ mm. The wavefront then becomes nearly planar again when approaching $x = 360 - 380$ mm. The sound field beyond that point will continue to be self-focused if the sample is long enough in the x direction. The

whole wave evolution process is rather indicative in the pressure field patterns given in Figs. 4(b), 4(d), and 4(f), following the expected sinusoidal trajectory in the proposed GRIN medium with a transverse hyperbolic secant refractive-index profile [52]. In view of the loss-induced refractive-index shift discussed in the Supplemental Material [54], it is fair to say that our design strategy is rather effective. For other frequencies near 1250 Hz, the sound fields are self-focused as well, but with varied focal length due to the dispersive nature of the refractive-index profile [54].

Since the result of the continuous GRIN medium is obtained based on two-dimensional bulk compressional-wave propagation while the actual SSAW is a surface mode traveling along the GRIN metasurface in three-dimensional space, a normalized comparison of sound energy densities becomes quite difficult. Hence, for the detailed acoustic-energy-density distributions across the focal spot [white dashed lines in Fig. 4(e)] as shown in Figs. 4(g) and 4(h), only the simulation and experimental results of the GRIN metasurface are presented. As anticipated, the highest peak, namely, the location of the focal spot, appears at about $x = 190$ mm in Fig. 4(g). The measured and simulated FWHMs are both 36 mm [red dotted lines in Fig. 4(h)], roughly $\lambda_0/7.6$, where $\lambda_0 = 274.4$ mm is the wavelength of free-space airborne sound at 1250 Hz. The measured acoustic-energy-density at the focal position is about 8.65 times greater than that obtained from the control experiment on a rigid plane surface [54], naturally lower than the 9.94 times acquired in simulation, but undoubtedly revealing an intensively focused and enhanced sound field. It is worth emphasizing that although the local-resonance-induced slow surface mode is crucial, the subwavelength focusing effect achieved here

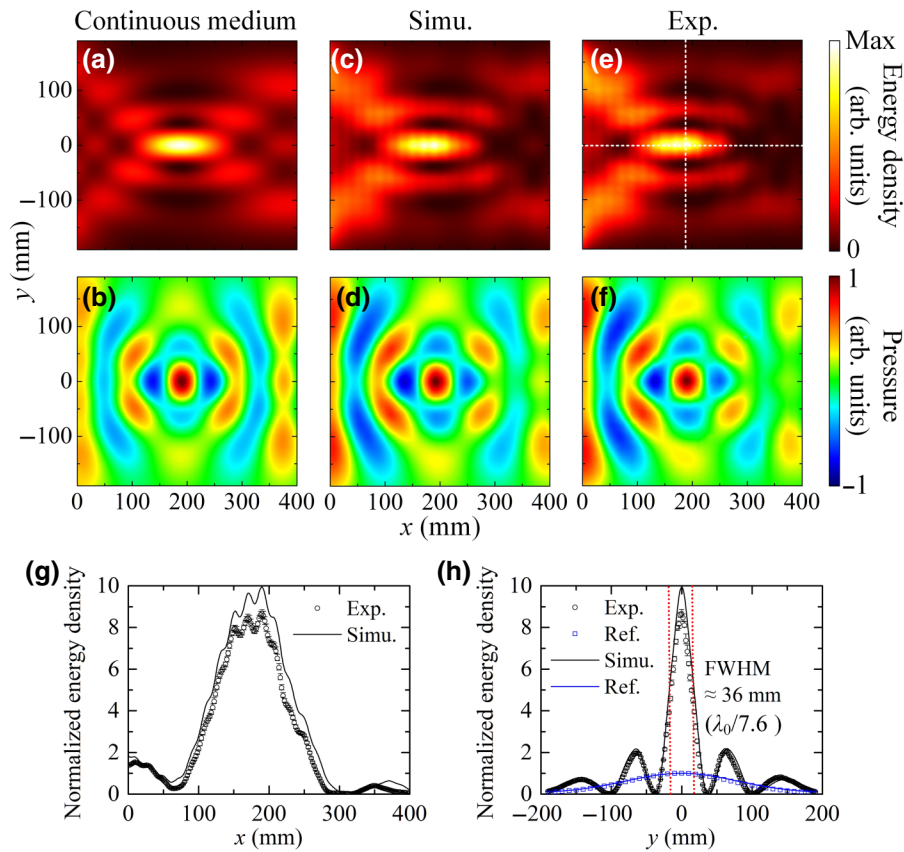


FIG. 4. Subwavelength focusing of airborne sound. (a),(b) Simulation result of a two-dimensional lossless continuous medium that respects the GRIN profile along the y direction. (c),(d) Simulation result of the GRIN metasurface. (e),(f) Corresponding experimental result. (a),(c),(e) are sound energy density fields; (b),(d),(f) are instantaneous pressure fields. The measurements are conducted 10 mm above the metasurface and the operating frequency is 1250 Hz. (g),(h) Normalized energy-density distributions along $y = 0$ and $x = 190$ mm. The white dashed lines in (e) mark where these curves are extracted. The results are normalized based on the referenced energy-density field along $x = 190$ mm [blue line and symbol in (h)] above a rigid plane surface [54]. The error bars are generated from five repeated measurements. A subwavelength focal spot is observed, which has 8.65-times-enhanced energy density and a FWHM of $\lambda_0/7.6$.

is not based on time reversal [22] or array shape [25], but is rather assisted by our systematically designed GRIN profile. This also breaks the restriction that the self-focusing effect has to happen inside a GRIN medium or a high-refractive-index immersion lens [56], as the near-field high-spatial-frequency information carried by the airborne SSAWs is measurable in the open environment above the metasurface [54]. Note that the decay of the SSAWs away from the metasurface is associated with their effective wavelength and thus, for practical applications, should be controlled to a relatively low value to facilitate the near-field measurement.

One may notice that the focal spot is “surprisingly” smaller than half the minimum effective wavelength of the SSAWs, $\lambda_s = 2\pi/q \approx 87.7$ mm. This seemingly unreasonable phenomenon is due to two facts. First, the overall effective refractive indices are underestimated in the lossless theoretical model of Eq. (2), namely, their actual values (in the presence of the inherent thermal and viscous losses) should be slightly higher than our initial design [54]. Second, the energy-density field within the opening area of a unit cell, namely, the inlet of the resonator, is stronger than that of its remaining area, which is especially obvious for lower measuring heights [54]. Consequently, the sharpened focal spot leads to the small FWHM in Fig. 4(h). As has been pointed out by Refs. [22] and [25], the FWHM here is associated with but not

equivalent to the minimum spatial resolution, and the latter is determined by the highest effective refractive index of the SSAWs.

VI. TWO-DIMENSIONAL SUBWAVELENGTH IMAGING

Evanescent waves play an essential role in super-resolution acoustic imaging. They carry rich subwavelength information, but decay exponentially away from the source. As we have demonstrated above, our acoustic metasurface is capable of coupling the nonpropagative evanescent components into the propagating SSAWs. Therefore, the information of high spatial frequency can be well preserved. One can also conclude that our GRIN acoustic metasurface should offer subwavelength imaging capability. To test this idea, we experimentally examine the sound field subject to: (1) a single pointlike imaging source; (2) a pair of in-phase pointlike imaging sources; and (3) a pair of out-of-phase pointlike imaging sources. All sources are 10×10 mm² in size, which can be regarded as a point compared to the wavelength in air.

As shown in Fig. 5(a), the SSAW wavefront from a single pointlike source is modulated by the GRIN metasurface and refocused in the opposite side of the y axis at about $x = 340 - 360$ mm, forming an inverted image with subwavelength features. Such imaging capability can be

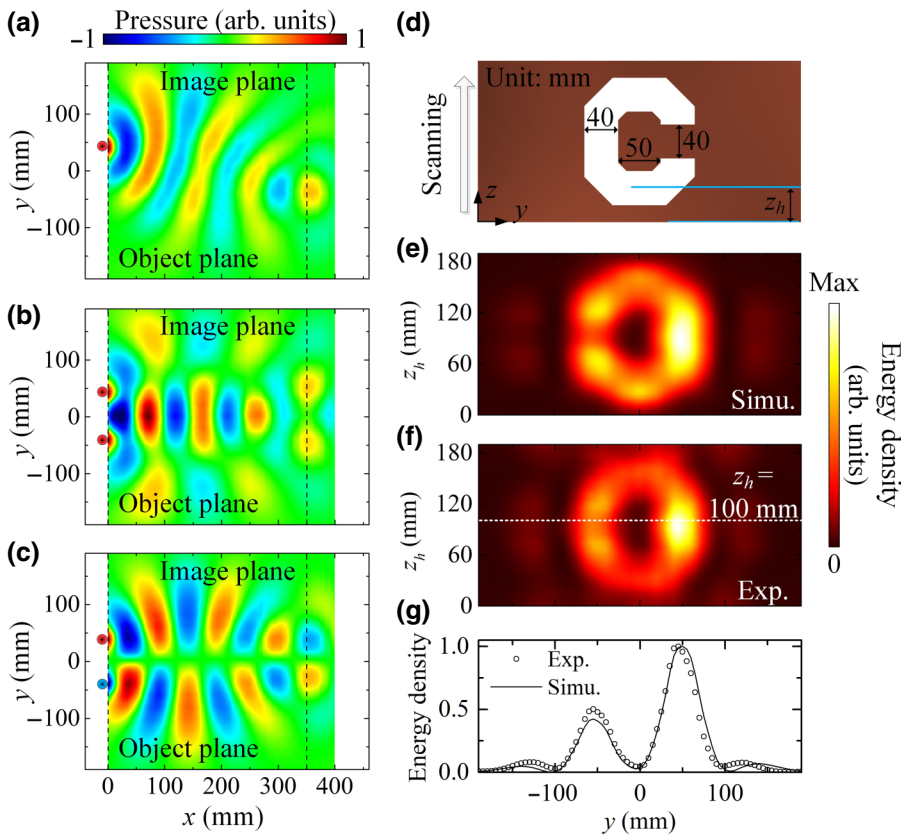


FIG. 5. Two-dimensional subwavelength imaging. Measured acoustic pressure fields at 1250 Hz subject to: (a) a single pointlike source; (b) a pair of in-phase pointlike sources; (c) a pair of out-of-phase pointlike sources. The solid circles are the pointlike sources, with colors denoting their phases. The object and image planes are marked by the black dashed lines. (d) C-shaped object plane. The scanning is conducted along the z direction. (e),(f) Synthesized images acquired through simulation and experiments. The images are synthesized by combining all the energy-density distributions obtained at different scanning heights z_h . (g) Normalized energy-density distribution for $z_h = 100$ mm. The location of $z_h = 100$ mm is marked by dashed white line in (f). The circles and solid line denote experimental and simulation results, respectively.

seen in Figs. 5(b) and 5(c), in which we further present the acoustic-pressure-field evolution induced by a pair of in-phase and out-of-phase pointlike sources. The center-to-center distance between the two sources is 80 mm, approximately $\lambda_0/3.4$ at 1250 Hz. The reconstructed images of the two pointlike sources, in both cases, are clearly distinguishable at the image plane [dashed lines in Figs. 5(a)–5(c)] after propagating along the GRIN metasurface. This image plane slightly shifts toward the object plane ($x = 0$) compared with the numerically acquired one [54]. It is possibly caused by the near-surface boundary layer losses, the environmental factors, the fabrication errors, and so on.

Subwavelength acoustic imaging of two-dimensional objects using the same GRIN acoustic metasurface sample is also demonstrated. The enhanced sound field is confined to the metasurface and attenuates exponentially with the increase of z , whose pressure amplitude drops to $1/e$ about 13 mm away from the surface at 1250 Hz [54]. Although only the evanescent components near the metasurface can be effectively coupled to the propagative SSAWs, we can accomplish two-dimensional imaging by moving the object along the z direction. After scanning the object plane at different scanning heights z_h [Fig. 5(d)], we can synthesize the measured energy density distributions to form the final image. A letter “C” with subwavelength geometrical features as shown in Fig. 5(d) is used as a

representative target. The simulated and measured images are presented in Figs. 5(e) and 5(f), respectively. Most subwavelength features of the C-shaped object, for example, edges and gaps, are successfully rebuilt in the synthesized image plane.

VII. DISCUSSION

We propose a straightforward design strategy of GRIN acoustic metasurfaces for the subwavelength manipulation of airborne sound by explicitly correlating the effective refractive index of spoof surface acoustic waves (SSAWs) with the unit-cell hole depth. The design procedure is much simplified, benefitting from avoiding massive time-consuming calculations. Meanwhile, the hole-depth-governed local-resonance behavior plays a key role in the broad adjustable range of the in-plane wave-vector value and thus the subwavelength feature. Subwavelength focusing of a plane acoustic wave, together with subwavelength sound imaging, are experimentally demonstrated with one GRIN acoustic metasurface sample. The presented GRIN metasurface is capable of performing spatial Fourier transform of acoustic waves at subwavelength scales. It may serve as a key element to miniaturize metamaterial-based analog computing devices [27–29] by taking full advantage of the SSAW, or even go a step further to integrate with Rayleigh-wave-based surface acoustic wave devices.

Other GRIN-enabled devices [57] such as acoustic Eaton lens, Luneburg lens, Maxwell-fish-eye lens, and black hole, or functionalities such as airy beam and Talbot effect under conformal transformation [58], can also be conveniently realized following the design strategy. It is not difficult to imagine that a better performance would become accessible if space-coiling [59,60] or helical-structured [61] acoustic metamaterials are adopted during the unit-cell design. In addition, this acoustic metasurface system is open to the surrounding environment with the enhanced sound field measurable even at a certain range away from the structure. It is, therefore, an ideal platform to directly observe and study how acoustic wave behaviors can be modulated by different exotic refractive-index distributions. For instance, the phenomenon of backscattering-immune wave guiding in an acoustic topological insulator [48] or unidirectional reflectionless propagation in a passive acoustic parity-time-symmetric medium [62] can be experimentally “visualized” in the subwavelength regime through measuring the spoof surface acoustic mode, which remains difficult for bulk composites or structures. Moreover, the nonleaky slow surface mode can further be coupled into a radiative mode, or vice versa, based on wave-vector matching via acoustic antennas [45,46]. Our findings will enable more flexible ways of sound manipulation and open additional possibilities for innovative applications for acoustic focusing, imaging, and sensing at subwavelength scales.

ACKNOWLEDGMENTS

This work was supported by the National Natural Science Foundation of China (Grant No. 11774297) and the university research Grant No. G-YBNT from the Hong Kong Polytechnic University.

-
- [1] J. B. Pendry, Negative Refraction Makes a Perfect Lens, *Phys. Rev. Lett.* **85**, 3966 (2000).
 - [2] N. Fang, H. Lee, C. Sun, and X. Zhang, Sub-diffraction-limited optical imaging with a silver superlens, *Science* **308**, 534 (2005).
 - [3] Z. Jacob, L. V. Alekseyev, and E. Narimanov, Optical Hyperlens: Far-field imaging beyond the diffraction limit, *Opt. Express* **14**, 8247 (2006).
 - [4] A. Salandrino and N. Engheta, Far-field subdiffraction optical microscopy using metamaterial crystals: Theory and simulations, *Phys. Rev. B* **74**, 075103 (2006).
 - [5] Z. Liu, H. Lee, Y. Xiong, C. Sun, and X. Zhang, Far-field optical hyperlens magnifying sub-diffraction-limited objects, *Science* **315**, 1686 (2007).
 - [6] M. Ambati, N. Fang, C. Sun, and X. Zhang, Surface resonant states and superlensing in acoustic metamaterials, *Phys. Rev. B* **75**, 195447 (2007).
 - [7] S. Guenneau, A. Movchan, G. Petursson, and S. A. Ramakrishna, Acoustic metamaterials for sound focusing and confinement, *New J. Phys.* **9**, 399 (2007).
 - [8] K. Deng, Y. Q. Ding, Z. J. He, H. P. Zhao, J. Shi, and Z. Y. Liu, Theoretical study of subwavelength imaging by acoustic metamaterial slabs, *J. Appl. Phys.* **105**, 124909 (2009).
 - [9] X. M. Zhou, M. B. Assouar, and M. Oudich, Sub-wavelength acoustic focusing by surface-wave-resonance enhanced transmission in doubly negative acoustic metamaterials, *J. Appl. Phys.* **116**, 194501 (2014).
 - [10] N. Kaina, F. Lemoult, M. Fink, and G. Lerosey, Negative refractive index and acoustic superlens from multiple scattering in single negative metamaterials, *Nature* **525**, 77 (2015).
 - [11] J. J. Park, C. M. Park, K. J. B. Lee, and S. H. Lee, Acoustic superlens using membrane-based metamaterials, *Appl. Phys. Lett.* **106**, 051901 (2015).
 - [12] X. Ao and C. T. Chan, Far-field image magnification for acoustic waves using anisotropic acoustic metamaterials, *Phys. Rev. E* **77**, 025601 (2008).
 - [13] J. Li, L. Fok, X. Yin, G. Bartal, and X. Zhang, Experimental demonstration of an acoustic magnifying hyperlens, *Nat. Mater.* **8**, 931 (2009).
 - [14] H. Jia, M. Z. Ke, R. Hao, Y. T. Ye, F. M. Liu, and Z. Y. Liu, Subwavelength imaging by a simple planar acoustic superlens, *Appl. Phys. Lett.* **97**, 173507 (2010).
 - [15] J. Zhu, J. Christensen, J. Jung, L. Martin-Moreno, X. Yin, L. Fok, X. Zhang, and F. J. Garcia-Vidal, A holey-structured metamaterial for acoustic deep-subwavelength imaging, *Nat Phys.* **7**, 52 (2010).
 - [16] X. M. Zhou and G. K. Hu, Superlensing effect of an anisotropic metamaterial slab with near-zero dynamic mass, *Appl. Phys. Lett.* **98**, 263510 (2011).
 - [17] J. Christensen and F. J. Garcia de Abajo, Anisotropic Metamaterials for Full Control of Acoustic Waves, *Phys. Rev. Lett.* **108**, 124301 (2012).
 - [18] Y. Cheng, C. Zhou, Q. Wei, D. J. Wu, and X. J. Liu, Acoustic subwavelength imaging of subsurface objects with acoustic resonant metalens, *Appl. Phys. Lett.* **103**, 224104 (2013).
 - [19] C. Shen, Y. Xie, N. Sui, W. Wang, S. A. Cummer, and Y. Jing, Broadband Acoustic Hyperbolic Metamaterial, *Phys. Rev. Lett.* **115**, 254301 (2015).
 - [20] G. Y. Song, W. X. Jiang, Q. Cheng, L. T. Wu, H. Y. Dong, and T. J. Cui, Acoustic magnifying lens for far-field high resolution imaging based on transformation acoustics, *Adv. Mater. Technol.* **2**, 1700089 (2017).
 - [21] J. de Rosny and M. Fink, Overcoming the Diffraction Limit in Wave Physics Using a Time-Reversal Mirror and a Novel Acoustic Sink, *Phys. Rev. Lett.* **89**, 124301 (2002).
 - [22] F. Lemoult, M. Fink, and G. Lerosey, Acoustic Resonators for Far-Field Control of Sound on a Subwavelength Scale, *Phys. Rev. Lett.* **107**, 064301 (2011).
 - [23] G. Ma, X. Fan, F. Ma, J. de Rosny, P. Sheng, and M. Fink, Towards anti-causal Green’s function for three-dimensional sub-diffraction focusing, *Nat. Phys.* **14**, 608 (2018).
 - [24] M. Moleron and C. Daraio, Acoustic metamaterial for subwavelength edge detection, *Nat. Commun.* **6**, 8037 (2015).

- [25] A. A. Maznev, G. Gu, S. Y. Sun, J. Xu, Y. Shen, N. Fang, and S. Y. Zhang, Extraordinary focusing of sound above a soda can array without time reversal, *New J. Phys.* **17**, 042001 (2015).
- [26] A. A. Maznev and O. B. Wright, Upholding the diffraction limit in the focusing of light and sound, *Wave Motion* **68**, 182 (2017).
- [27] A. Silva, F. Monticone, G. Castaldi, V. Galdi, A. Alu, and N. Engheta, Performing mathematical operations with metamaterials, *Science* **343**, 160 (2014).
- [28] S. Y. Zuo, Q. Wei, Y. Cheng, and X. J. Liu, Mathematical operations for acoustic signals based on layered labyrinthine metasurfaces, *Appl. Phys. Lett.* **110**, 011904 (2017).
- [29] F. Z. Nejad and R. Fleury, Performing mathematical operations using high-index acoustic metamaterials, *New J. Phys.* **20**, 073001 (2018).
- [30] J. B. Pendry, L. Martin-Moreno, and F. J. Garcia-Vidal, Mimicking surface plasmons with structured surfaces, *Science* **305**, 847 (2004).
- [31] A. P. Hibbins, B. R. Evans, and J. R. Sambles, Experimental verification of designer surface plasmons, *Science* **308**, 670 (2005).
- [32] L. Kelders, J. F. Allard, and W. Lauriks, Ultrasonic surface waves above rectangular-groove gratings, *J. Acoust. Soc. Am.* **103**, 2730 (1998).
- [33] J. Christensen, A. I. Fernandez-Dominguez, F. De Leon-Perez, L. Martin-Moreno, and F. J. Garcia-Vidal, Collimation of sound assisted by acoustic surface waves, *Nat. Phys.* **3**, 851 (2007).
- [34] J. Christensen, P. A. Huidobro, L. Martin-Moreno, and F. J. Garcia-Vidal, Confining and slowing airborne sound with a corrugated metawire, *Appl. Phys. Lett.* **93**, 083502 (2008).
- [35] Y. Zhou, M. H. Lu, L. Feng, X. Ni, Y. F. Chen, Y. Y. Zhu, S. N. Zhu, and N. B. Ming, Acoustic Surface Evanescent Wave and its Dominant Contribution to Extraordinary Acoustic Transmission and Collimation of Sound, *Phys. Rev. Lett.* **104**, 164301 (2010).
- [36] Z. J. He, H. Jia, C. Y. Qiu, Y. T. Ye, R. Hao, M. Z. Ke, and Z. Y. Liu, Nonleaky surface acoustic waves on a textured rigid surface, *Phys. Rev. B* **83**, 132101 (2011).
- [37] D. Torrent and J. Sanchez-Dehesa, Acoustic Analogue of Graphene: Observation of Dirac Cones in Acoustic Surface Waves, *Phys. Rev. Lett.* **108**, 174301 (2012).
- [38] H. Jia, M. H. Lu, Q. C. Wang, M. Bao, and X. D. Li, Sub-wavelength imaging through spoof surface acoustic waves on a two-dimensional structured rigid surface, *Appl. Phys. Lett.* **103**, 103505 (2013).
- [39] Y. T. Ye, M. Z. Ke, Y. X. Li, T. Wang, and Z. Y. Liu, Focusing of spoof surface-acoustic-waves by a gradient-index structure, *J. Appl. Phys.* **114**, 154504 (2013).
- [40] J. Zhu, Y. Y. Chen, X. F. Zhu, F. J. Garcia-Vidal, X. B. Yin, W. L. Zhang, and X. Zhang, Acoustic rainbow trapping, *Sci. Rep.* **3**, 01728 (2013).
- [41] Y. Chen, H. Liu, M. Reilly, H. Bae, and M. Yu, Enhanced acoustic sensing through wave compression and pressure amplification in anisotropic metamaterials, *Nat. Commun.* **5**, 5247 (2014).
- [42] H. Jia, M. H. Lu, X. Ni, M. Bao, and X. D. Li, Spatial separation of spoof surface acoustic waves on the graded groove grating, *J. Appl. Phys.* **116**, 124504 (2014).
- [43] L. Quan, X. Zhong, X. Liu, X. Gong, and P. A. Johnson, Effective impedance boundary optimization and its contribution to dipole radiation and radiation pattern control, *Nat. Commun.* **5**, 3188 (2014).
- [44] J. Y. Lu, C. Y. Qiu, M. Z. Ke, and Z. Y. Liu, Directional excitation of the designer surface acoustic waves, *Appl. Phys. Lett.* **106**, 201901 (2015).
- [45] L. Quan, F. Qian, X. Z. Liu, X. F. Gong, and P. A. Johnson, Mimicking surface plasmons in acoustics at low frequency, *Phys. Rev. B* **92**, 104105 (2015).
- [46] J. Cui, J. H. Liu, Y. W. Mao, Y. F. Li, and X. Z. Liu, Realization of manipulating acoustic surface waves radiation direction with rectangular-groove structure, *AIP Adv.* **7**, 115301 (2017).
- [47] L. Schwan, A. Geslain, V. Romero-Garcia, and J. P. Groby, Complex dispersion relation of surface acoustic waves at a lossy metasurface, *Appl. Phys. Lett.* **110**, 051902 (2017).
- [48] S. Yves, R. Fleury, F. Lemoult, M. Fink, and G. Lerosey, Topological acoustic polaritons: robust sound manipulation at the subwavelength scale, *New J. Phys.* **19**, 075003 (2017).
- [49] T. Liu, S. Liang, F. Chen, and J. Zhu, Inherent losses induced absorptive acoustic rainbow trapping with a gradient metasurface, *J. Appl. Phys.* **123**, 091702 (2018).
- [50] L. T. Wu, G. Y. Song, W. K. Cao, Q. Cheng, T. J. Cui, and Y. Jing, Generation of multiband spoof surface acoustic waves via high-order modes, *Phys. Rev. B* **97**, 214305 (2018).
- [51] W. K. Cao, L. T. Wu, C. Zhang, G. Y. Song, J. C. Ke, Q. Cheng, and T. J. Cui, Acoustic surface waves on three-dimensional groove gratings with sub-wavelength thickness, *Appl. Phys. Express* **11**, 087301 (2018).
- [52] S.-C. S. Lin, T. J. Huang, J.-H. Sun, and T.-T. Wu, Gradient-index phononic crystals, *Phys. Rev. B* **79**, 094302 (2009).
- [53] A. Climente, D. Torrent, and J. Sanchez-Dehesa, Sound focusing by gradient index sonic lenses, *Appl. Phys. Lett.* **97**, 104103 (2010).
- [54] See Supplemental Material at <http://link.aps.org/supplemental/10.1103/PhysRevApplied.11.034061> for a discussion of the inherent visco-thermal losses, a schematic illustration of the experimental setup, the control experiment, the measured energy density fields at different frequencies, the measured energy density fields at different height, and the simulated acoustic pressure fields generated by point-like source(s).
- [55] M. Amin, O. Siddiqui, M. Farhat, and A. Khelif, A perfect Fresnel acoustic reflector implemented by a Fano-resonant metascreen, *J. Appl. Phys.* **123**, 144502 (2018).
- [56] S. M. Mansfield and G. S. Kino, Solid immersion microscope, *Appl. Phys. Lett.* **57**, 2615 (1990).
- [57] T. M. Chang, G. Dupont, S. Enoch, and S. Guenneau, Enhanced control of light and sound trajectories with three-dimensional gradient index lenses, *New J. Phys.* **14**, 035011 (2012).
- [58] X. Wang, H. Chen, H. Liu, L. Xu, C. Sheng, and S. Zhu, Self-Focusing and the Talbot Effect in Conformal Transformation Optics, *Phys. Rev. Lett.* **119**, 033902 (2017).

- [59] Z. Liang and J. Li, Extreme Acoustic Metamaterial by Coiling up Space, *Phys. Rev. Lett.* **108**, 114301 (2012).
- [60] Y. Li, B. Liang, X. Tao, X. F. Zhu, X. Y. Zou, and J. C. Cheng, Acoustic focusing by coiling up space, *Appl. Phys. Lett.* **101**, 233508 (2012).
- [61] X. Zhu, K. Li, P. Zhang, J. Zhu, J. Zhang, C. Tian, and S. Liu, Implementation of dispersion-free slow acoustic wave propagation and phase engineering with helical-structured metamaterials, *Nat. Commun.* **7**, 11731 (2016).
- [62] T. Liu, X. Zhu, F. Chen, S. Liang, and J. Zhu, Unidirectional Wave Vector Manipulation in Two-Dimensional Space With an All Passive Acoustic Parity-Time-Symmetric Metamaterials Crystal, *Phys. Rev. Lett.* **120**, 124502 (2018).